Radiation Detection Technology and Methods (2022) 6:234–243
https://doi.org/10.1007/s41605-022-00315-7

ORIGINAL PAPER

Neutron transmission imaging with a portable D-T neutron generator

Phillip Kerr[1] · Nerine Cherepy[1] · Jennifer Church[1] · Gary Guethlein[1] · Jim Hall[1] · Colby McNamee[1] · Sean O'Neal[1] · Kyle Champley[1] · Andy Townsend[1] · Mayuki Sasagawa[1] · Anthony Hardy[1] · Saphon Hok[1]

Received: 29 September 2021 / Revised: 22 December 2021 / Accepted: 30 December 2021 / Published online: 27 February 2022

Abstract

Purpose A portable fast-neutron imaging system is being developed to provide complementary information to field X-ray imaging. Applications include inspection of vehicles and infrastructure for corrosion, measurement of material levels in containers, and inspection of munitions and suspicious packages. While fast-neuron imaging generally provides lower imaging resolution compared to X-rays, fast-neutron interaction cross-sections have a weak dependence on material Z. This enables imaging of low-Z materials inside high-Z materials. Here, we discuss the limitations and current improvements in fast-neuron imaging.

Methods Limitations in portable fast-neutron imaging systems include low D-T neutron generator output, low light production in ZnS(Cu) imaging scintillators, low resolution due to scintillator thickness and D-T spot size, and digital-panel darknoise that varies in time and position and that can be 100× larger than the neutron signal. We have made improvements in these areas through development of a segmented high light yield scintillator, panel noise mitigation techniques, and testing of new high-output, small spot size D-T neutron generators.

Results The segmented high light yield fast-neutron scintillator demonstrated 5× increase in light compared to ZnS(Cu). An additional 2× improvement in signal-to-noise was demonstrated with panel-noise mitigation techniques. Our MCNP calculations also show good agreement with neutron imaging results

Conclusions We have demonstrated improvements in fast-neutron imaging through development of a segmented high light yield neutron scintillator, mitigation of digital panel noise, and preliminary testing with new high-output, small spot size D-T neutron generators. We have also demonstrated good results modeling fast-neutron images and scatter effects using MCNP.

Keywords Fast-neutron radiography · Portable neutron imaging · Neutron scintillators · Monte Carlo simulation

Introduction

The state-of-the-art for a fieldable imaging system is based on portable X-ray machines and digital imaging panels or phosphor screens. While X-rays can produce high-spatial-resolution radiographs, they have limited penetration power for dense, heavily shielded objects. Efforts to image low-Z materials inside high-Z materials with X-rays tend to overexpose the low-Z materials and obscure details [1]. Fast-neutron imaging broadens the type and size of objects that can be imaged in the field. Compared to X-rays, fast-neutron interaction cross-sections have a weak dependence on material Z and tend to produce images with more uniform contrast as a function of material. Fast neutrons, such as those from a portable D-T neutron generator, therefore enable imaging of low-Z materials inside high-Z materials. Fast neutron imaging provides complementary information to X-ray imaging. In the words of Klann [2], "The key is that contrast between high-Z and low-Z materials is too extreme for X-rays, therefore, large changes in density or material cannot be viewed simultaneously with X-rays due to a large change in the mass attenuation coefficient, μ/ρ. Whereas, for fast neutrons, the total cross-section does not vary significantly so these regions can be viewed simultaneously."

Neutron imaging has application for specific end-user applications, including those involved in nuclear incident response, treaty verification, and industrial or defense inspections. Currently, available neutron imaging systems are typically thermal neutron imagers based at nuclear reactors or other large installations and are not suitable for field use.

✉ Phillip Kerr
Kerr12@Llnl.Gov

[1] Lawrence Livermore National Laboratory, Livermore, CA 94550, USA

Fast-neutron radiography has been utilized, but to a lesser extent than thermal neutron radiography, and is also typically performed at reactors [3]. However, there is now increasing interest in fast-neutron radiography as a diagnostics tool [1–7]. This has been accompanied by the development of dedicated D-T neutron generator imaging installations and the development of portable high-output, small spot size D-T neutron generators. The latter allows the potential for field neutron radiography.

The time, distance, and shielding safety requirements for field neutron radiography can be very different for different applications. For routine inspections near populated areas, significant shielding or standoff distance may be required and may not always be practical. In other applications, operators may be prepared for the high dose from D-T neutron generators depending on the conditions and demands of the operation. The isotropic dose rate at 1 m for a 1.0×10^{10} n/s D-T neutron generator is about 0.1 Sv/hr. For comparison, a commercial 7 MeV SEA-7 Betatron, often used for field radiography, is 6 Sv/hr in front and 0.3 Sv/hr behind. The unshielded standoff distance for D-T neutron radiography is therefore comparable to or less than that used for portable 7 MeV Betatron radiography. Shielding materials and masses would typically differ, with concrete and borated plastics employed for neutron shielding and lead and steel employed for X-ray shielding.

In this paper, we discuss development of a portable neutron transmission imaging system suitable for field use. The goal of the research is to enhance imaging capability in the field beyond that provided by X-ray imaging alone. Preliminary work with commercial portable neutron sources and imaging panels demonstrated that improvement in the signal-to-noise (S/N) of about 100 × is needed to develop a practical field neutron radiography system. More specifically, this requires improvements in neutron source output, spot size, and neutron scintillator light production and detection. Here we discuss efforts to improve upon the S/N from the preliminary work using a newly-developed segmented high light-yield plastic scintillator, implementing techniques to mitigate digital panel noise, and integrating a newly available high-output, small spot size portable D-T neutron generator. We also discuss MCNP modeling of the neutron imaging system to better understand the scintillator resolution and neutron scatter contribution to image quality.

Experimental data

The experimental fast-neutron transmission imaging results detailed here use a Thermo Scientific P 385 DT neutron generator, Varex Imaging XRD 1621 digital TFT imaging panel, and an RC Tritec 2.4 mm thick ZnS(Cu) scintillator screen.

Fig. 1 Thermo scientific P 385 neutron generator

Neutron source

The fast neutron radiographs presented here were obtained using a Thermo Scientific P 385 DT neutron generator as shown in Fig. 1. Neutrons are generated via the D-T reaction by accelerating deuterons through 130 kV to a tritiated titanium target with a deuteron beam current of 70 μA. The D-T reaction produces 14.1 MeV neutrons at 90° to the beam axis. The P 385 generator was operated in continuous mode at the maximum output of 5.9×10^8 n/s. The generator is warranted to 1200 h. at 3e8 n/s output. The neutrons are emitted almost isotropically, resulting in point-source or cone-beam imaging. In practice, the neutrons are emitted from a circular region on the titanium target with a full-width half-maximum (FWHM) spot size of about 7–10 mm.

The angular distribution of neutron output was calculated using MCNP and measured using a 10.16 cm diameter × 7.62 cm thick EJ-301 xylene-base liquid scintillator detector to determine an optimal imaging angle in terms of uniformity and magnitude of flux. Figure 2 shows a plot of the P 385 neutron angular distribution calculated from MCNP (left) and measured (right). Figure 3 shows the two-dimensional pulse-shape discrimination plot of DT neutrons from the detector. The high-energy neutron region-of-interest shown is sensitive to just direct neutrons from the P 385.

The recent U.S. Department of Defense (DoD) Defense Advanced Research Projects Agency (DARPA) Intense Compact Neutron Source (ICONS) program funded industry to increase neutron generator output and reduce source spot size while keeping the generator highly portable. The Starfire Industries nGen-400-DT-P-VIPS source shown in Fig. 4 is anticipated to produce $> 5 \times 10^9$ n/s, with a 2 mm spot size, and weigh about 20 kg. This neutron generator is warranted for 12 months/500 h. We plan to utilize this > 10 × brighter source in the deployment of a fieldable neutron transmission imaging system.

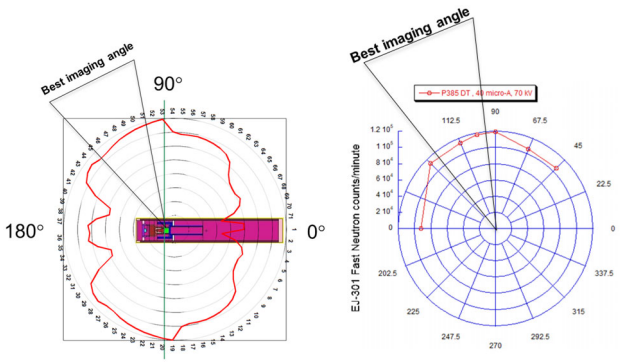

Fig. 2 Angular distribution of thermo scientific P 385 neutron output calculated with MCNP (left) and measured with an EJ-301 liquid scintillator detector (right). The DT source was oriented at 135° to provide a uniform neutron field. Note the emission angle towards the front of the tube (left side of plot) is kinematically 180° due to the ion acceleration in the tube being from left to right in the plot

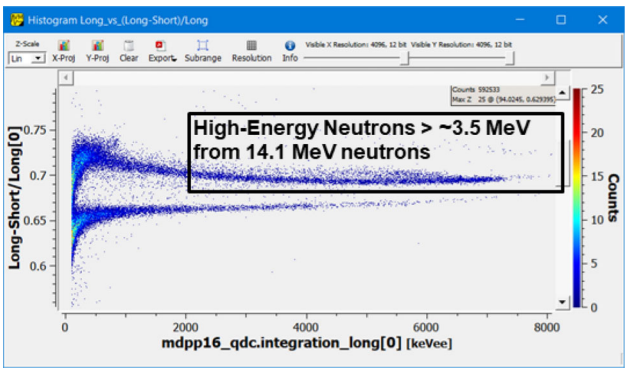

Fig. 3 Two-dimensional pulse-shape discrimination plot of gamma-rays (lower band) and DT neutrons (upper band) from a 10.16 cm diameter × 7.62 cm thick EJ-301 xylene-base liquid scintillator detector. The region-of-interest of high-energy neutrons used to measure flux as a function of angle is also indicated

Fig. 4 Conceptual rendering of the Starfire Industries nGen-400-DT-VIPS Sealed 14.1 MeV deuterium–tritium neutron generator

Digital panel and neutron scintillator

Neutron images were obtained using 2.4 mm thick ZnS(Cu) screen mounted on a 41 cm × 41 cm Perkin Elmer Varex XRD 1621 digital imaging silicon thin-film transistor (TFT) panel as shown in Fig. 5(left). The scintillator screen placed on the silicon surface (center) is an RC Tritec 400 mm × 400 mm FNR PP30 1 2400 scintillator sheet, which is 30 weight percent ZnS(Cu) on a high density and high transparency polypropylene (0.905 g/cc) backing. The light emission spectra are green at ~ 520 nm. The limiting element for resolution in the panel is the 2.4 mm ZnS(Cu) screen, so for data compression benefit, the 200 μm pixels were binned during acquisition into 400 μm × 400 μm elements. A 0.5 mm tantalum sheet (right) was placed in front of the scintillator to shield the 130 keV Bremsstrahlung X-rays produced in the neutron generator.

In an effort to improve the light output of the imaging system, we are developing a replacement for the ZnS(Cu) scintillator screen. While the ZnS(Cu) has a very high intrinsic light yield, it is not optically transparent to the resulting green light and has a maximum optimal thickness of about 2.4 mm. As a result, a high light yield scintillator SH-267 developed at Lawrence Livermore National Lab is being adapted to this application [9, 10]. This scintillator is optically transparent and can therefore be made much thicker. In order to maintain resolution comparable to the 2.4 mm ZnS(Cu) scintillator, the SH-267 scintillator must be segmented to a similar pixel dimension. Table 1shows a comparison of the anticipated light output of these two scintillators.

The technique being employed to segment the new scintillator is a saw cutting technique. We have demonstrated the ability to produce an array of 3 mm × 3 mm pixels in a 5 cm × 5 cm × 2.5 cm thick cube of SH-267. As a result, the total light output is expected to be about a factor of 5 higher. The cut grooves of two SH-267 cubes were filled with two optical reflective materials, Teflon and Vikuiti, for comparison.

Figure 6 shows the progression of testing the saw cut segmentation process. From left to right, photos of test cuts in a block of acrylic (1), Eljen EJ-200 plastic scintillator (2), and SH-267 (3) all with Teflon reflector in cut grooves. Shown next is SH-267 with top UV illumination (4), and side UV illumination (5) showing minimal light leakage. Image (6) shows a larger 10 cm x 10 cm plate of SH-267.

The two samples of SH-267 were then placed on the Varex XRD 1621 panel along with a 10 cm x 10 cm sample of ZnS(Cu) to measure the relative neutron light output of the scintillators from the P 385 DT neutron generator described above. Due to the height of the SH-267 samples and the limited space inside the XRD panel for a scintillator, an extension panel cover was constructed to accommodate the 2.5 cm tall samples. Results of the neutron light output can be

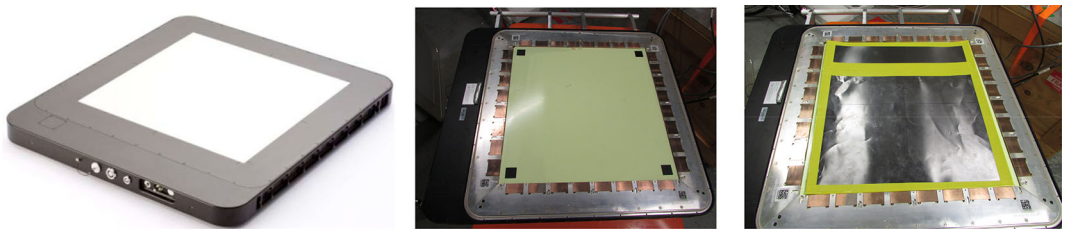

Fig. 5 Varex imaging XRD 1621 TFT digital imaging panel (left), with ZnS(Cu) scintillator screen mounted (center), and with 0.5 mm Ta sheet added for 130 keV X-ray shielding

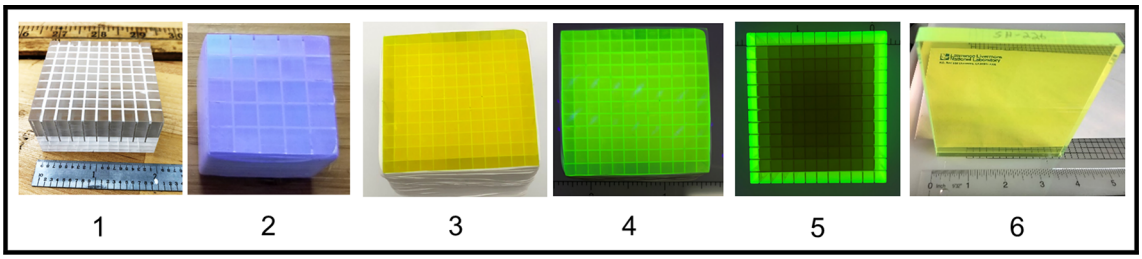

Fig. 6 Progression of segmented scintillator development: test cut groove segmentation in 5 cm × 5 cm articles of acrylic (1), Eljen EJ-20 (2), and SH-267 (3) all with Teflon reflector in cut grooves. Also shown is SH-267 with top UV illumination (4), and side UV illumination (5) showing minimal light leakage. Image (6) shows a larger 10 cm × 10 cm plate of SH-267

Table 1 Comparison of relative light yield, thickness, resolution, and total relative light from ZnS(Cu) and SH-267 showing about a factor of 5 × expected with SH-267

Scintillator	Light yield (relative)	Thickness (mm)	Estimated resolution (mm)	Total = light yield * thickness
ZnS:Cu in polypropylene	8	2.4	2.4 mm (limited by proton track length and light diffusion in screen)	19
SH-267 Plastic	4	25	3 mm (by voxel size)	100

seen in Fig. 7 with ZnS(Cu) at average 675 counts/pixel and the Teflon-filled SH-267 at 4122 counts/pixel. The source-to-panel distance was 50 cm and the exposure time was two minutes. This measured light yield demonstrates a 6 × increase with SH-267. The segmented SH-267 cube grooves were filled with either Teflon or Vikuiti optical reflective materials as indicated. The 3 mm x 3 mm pixels in the SH-267 sample neutron radiograph can be seen in the contrast adjusted Fig. 8.

The pixels are cut down to a base section that is less than 0.5 mm thick. The light leaks are very small due to the angular distribution of the photons that are transported in the 25 mm long pixels. Photons, therefore, have a low probability of being captured in the plane of the connected plastic at the base. The scintillation light is emitted into 4π , but the light that stays within the pixel due to total internal reflection is transported in the long dimension of the pixel and geometrically becomes directed into the amorphous Si region just beneath the pixel. Construction of a large array suitable for neutron cross talk testing and imaging is in progress. An

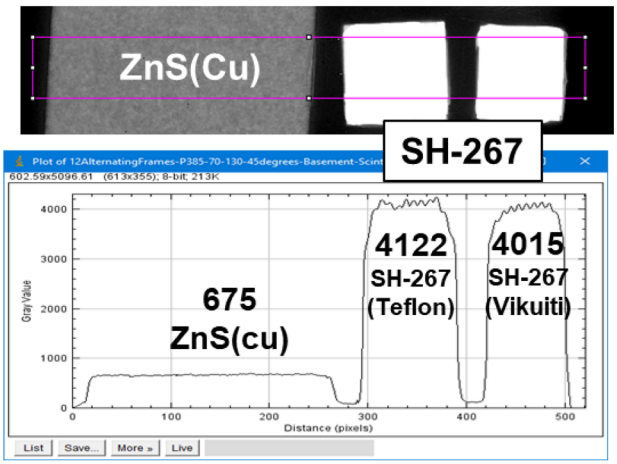

Fig. 7 Neutron radiograph and line out of the neutron light yield from a 2.4 mm thick ZnS(Cu) plate (left) compared to two segmented 5 cm × 5 cm × 2.5 cm SH-267 cubes. The segmented SH-267 cube grooves were filled with two types of optical reflective material, Teflon (center), and Vikuiti (right). The measured light yield demonstrates a 6 × increase using SH-267

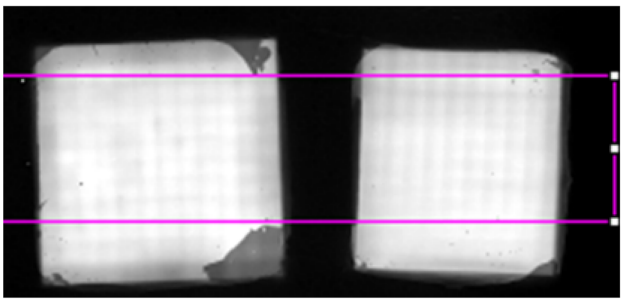

Fig. 8 Neutron radiograph of SH-267 samples with contrast adjusted to see 3 mm × 3 mm pixels

estimate of pixel light cross-talk is obtained from UV side illumination of the segmented scintillator indicating an upper bound of about 25%.

Image construction

Digital imaging TFT devices have an electronic dark noise background count rate that varies in time and position across the device. This variation is especially pronounced when the panel is first energized and becomes more uniform over a period of hours as the panel reaches thermal stability. Due to the low interaction rate of fast neutrons in ZnS(Cu) and the resulting low production of light, this dark noise is much larger than the neutron signal and requires special attention for extraction of images that is not necessary for X-ray imaging.

The process of image construction consists of several steps: 1.) the digital panel data-acquisition software is set to acquire multiple image frames of 20 s each, 2.) the neutron generator output is synchronized to the panel frame rate to obtain alternating active (neutron) and passive (dark noise) frames. This frequent background subtraction produces a higher signal-to-noise ratio than subtracting a long dark acquisition from a long active acquisition 3.) pairs of active and passive frames are subtracted from each other and successively added together to obtain the background-subtracted raw object image:

$$I_{\text{Obj}} - I_D = (N_1 - D_1) + (N_2 - D_2) + (N_3 - D_3) + \ldots (N_x - D_x) \quad (1)$$

where I_{obj} and I_D are the object image and dark image, respectively, N_x refers to a 20 s neutron (active) frame, and D_x refers to a 20 s dark (passive) frame. 4.) A background-subtracted open-field image is then obtained by repeating this process after moving the object away from the panel:

$$I_{\text{Open}} - I_D = (N_1 - D_1) + (N_2 - D_2) + (N_3 - D_3) + \ldots (N_x - D_x) \quad (2)$$

Table 2 Results of frame averaging techniques showing reduction of frame average (noise floor) and standard deviation getting closer to zero with odd–even frame averaging and additional corrections from corner noise knowledge

Dark subtraction method	Frame average	Standard deviation
First-last (1 + 2 + 3…− 10 − **11** − **12**)	− 672	180
Odd–even (1–2 + 3–4 … + 11 − 12)	− 111	35
Odd–even*4 corner weight	21	28
Odd–even*dot distance weight	− 3	24

The final flat-fielded image is obtained by dividing the object image by the open-field image:

$$I_{\text{flatfield}} = (I_{\text{Obj}} - I_D)/(I_{\text{Open}} - I_D) \quad (3)$$

The images in this report consist of 12 alternating frames, adding up to four minutes of runtime with two minutes of active frames and two minutes of passive frames.

In addition to the alternating frames averaging, four corners of the ZnS(Cu) scintillator screen were masked with black tape to allow monitoring of the dark noise in those areas during all active frames. Because the noise varies in time, monitoring the corners enables some ability to predict the dark noise across the full panel during active frames. Figure 9 shows the ZnS(Cu) screen with masked corners and progression of improving knowledge of the image noise floor with different frame averaging techniques. Table 2 shows the frame average (noise floor) of images resulting from the various techniques. The odd–even frame averaging combined with distance-weighted corner corrections results in a noise floor of close to zero with the smallest standard deviation. Compared to a first-last frame image construction, the techniques used here improve the signal-to-noise ratio in the images by a factor of three.

One additional correction is monitoring the total number of neutrons detected during each frame by an independent neutron detector near the neutron generator. Ideally, all active frames would have the same number of neutrons and all passive frames would have zero or background neutrons. In practice, neutron generators do not produce identical output in time, especially if the neutron generator is turned on and off every 20 s as in the current technique. Monitoring the output during each frame allows normalization of frames, particularly important when dividing the object and open field images to produce the flat fielded image.

Figure 10 provides a graphical depiction of the frame sequence used here during neutron acquisition and neutron

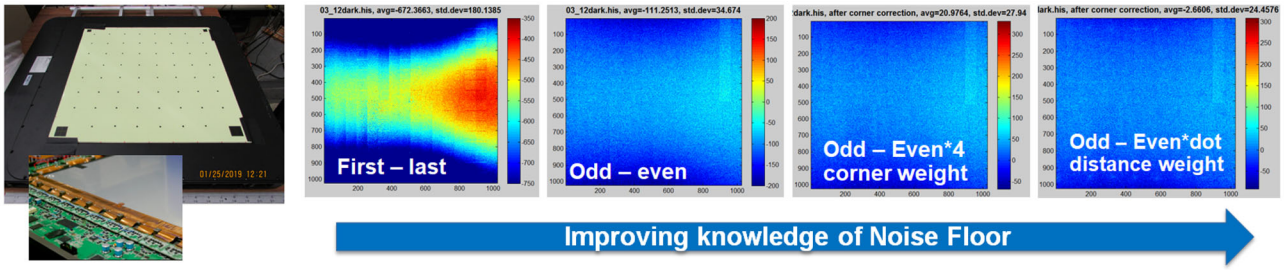

Fig. 9 Image of ZnS(Cu) screen with corner masking (left) and comparison of panel noise uniformity using four frame averaging techniques. The noise floor is lowest using odd–even frames weighted by distance and value of masked corners

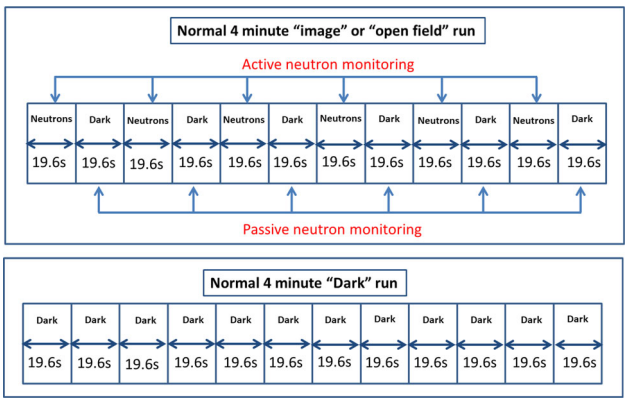

Fig. 10 Graphic showing the frame sequence of neutron acquisition and neutron monitoring for imaging (top) and dark runs (bottom)

monitoring for the object image (top) and dark image (bottom).

Experimental data

Neutron transmission images were obtained with the baseline system described above including a Thermo Scientific P 385 DT neutron generator, a Varex Imaging XRD 1621 digital imaging panel with 2.4 mm ZnS(Cu) scintillator screen, and a 0.5 mm tantalum sheet for shielding a small amount of 130 keV Bremsstrahlung X-rays produced by the neutron generator. The generator was placed at a 45° angle from the front (135° from ion source direction) for optimal neutron flux as shown in Fig. 2.

One of the primary radiography test objects (RTO's) imaged was an open-top, 12.7 cm diameter, 1.27 cm thick tungsten sphere containing a polyethylene cylinder. A schematic dimensional drawing of this object is shown in Figure 11 The source-to-detector (SD) distance was 61 cm and the object-to-detector (OD) distance was 31 cm for a magnification of about 2. The neutron imaging system was operated in a basement location 70 cm above a concrete floor and 100 cm from the nearest concrete wall. Figure 12 shows a photograph of the experimental setup. Figure 13 shows the flat-fielded neutron transmission image of this

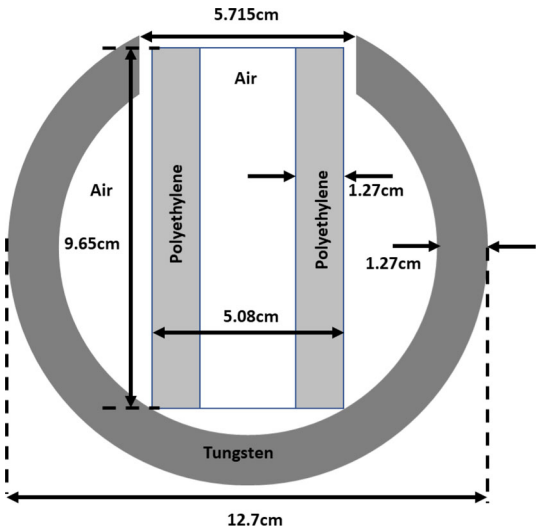

Fig. 11 Schematic dimensional drawing of spherical tungsten/polyethylene radiography test object

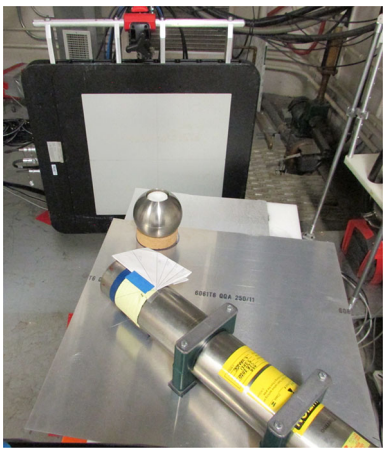

Fig. 12 Photograph of the experimental setup for fast-neutron transmission imaging of the tungsten/polyethylene radiography test object using the Thermo Scientific P 385 neutron generator and Varex imaging XRD 1621 digital imaging panel. The XRD panel contains a 2.4 mm ZnS(Cu) scintillator screen and a 0.5 cm thick tantalum X-ray shield

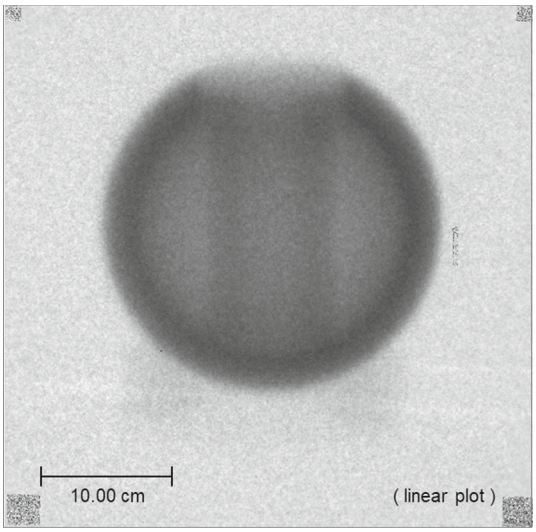

Fig. 13 Flat-fielded experimental image of tungsten/polyethylene radiography test object

RTO. Note that the polyethylene cylinder is clearly visible inside the tungsten sphere. Low-energy X-ray radiography, e.g. 450 keV, would provide a clearly defined edge of this object but no information on interior features.

Figure 14 shows a photograph (left) and neutron transmission image (center) of a tungsten and plastic RTO demonstrating the ability of fast neutrons to image low-Z materials behind high-Z materials. This test object consists of 4.8 cm tungsten shielding a 2.5 cm wide × 6.35 cm deep block of plastic. The image on the right side of the figure is a plot profile line-out showing a 50% contrast through the tungsten and a 37% contrast through the tungsten and plastic. Notice in the grayscale transmission image (center) that the high-Z material appears to attenuate more than an equivalent thickness of a low-Z material for high-energy neutron radiography. The 4.8 cm tungsten region is 130 cts/pixel and the thicker 6.35 cm plastic above the tungsten is higher at 175 cts/pixel. This may be counter-intuitive if basing on low-energy neutron radiography and or neutron capture. With D-T neutrons, very few are captured in the object. The 'attenuation' apparent in the image is due to neutrons that have been scattered away by the object. The image *signal* is attenuated, but the neutrons are not actually attenuated, they are mostly deflected. Contrast of high-energy neutron radiographic images is more dependent on neutron deflection in the object than on neutron capture since the image recording relies on proton recoil. Contrast is also therefore insensitive to thermal neutrons.

Another RTO is the XRO5 shown in Fig. 15. The layers of this object consist of a polyethylene center, brass cylinder, titanium cylinder, polyethylene cylinder, and aluminum cylinder with various machined grooves. The DT source was placed again at 45°. The source to detector distance was 50 cm and the object to detector distance was 8.5 cm to minimize the effect of the source spot size on resolution. This object was imaged in 45 views spaced 8° apart to produce a CT data set. A CT reconstruction using Livermore Tomography Tools (LTT) is shown in Fig. 16 [11].

Monte-Carlo simulations

Monte Carlo simulations of our imaging experiment were conducted using MCNP 6.2. The FMESH01:n tally was used along with accurate models of the XRD 1621 panel, scintillator screen, support structures, room floor, ceiling, and walls, and the P 385 neutron generator tube. The panel was modeled as a 1024 × 1024 array of 400 μm pixel pitch, along with a detailed detector response function for the 2.4 mm ZnS(Cu)

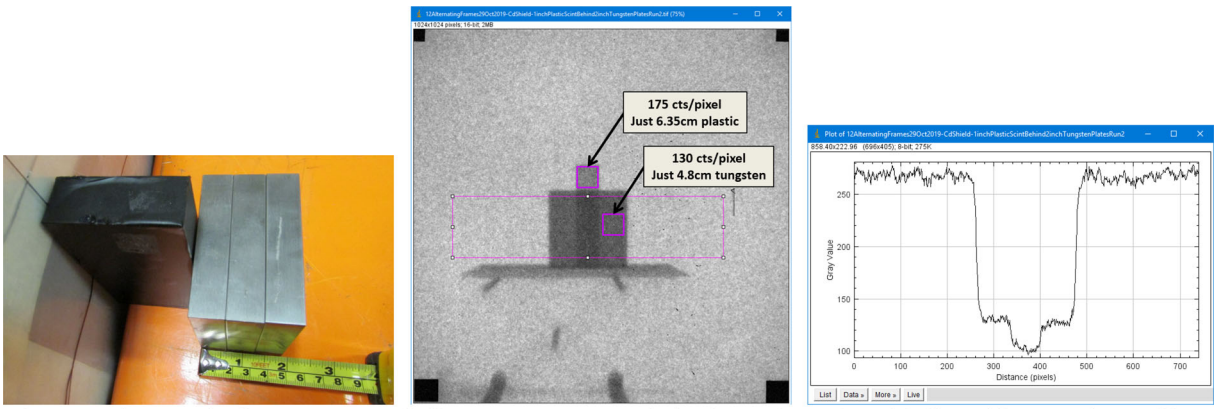

Fig. 14 Photograph of a neutron RTO (left), raw neutron transmission image (center), and indicated line-out plot profile (right). The RTO consists of 4.8 cm of tungsten blocks in front of a 2.54 cm wide × 6.35 cm deep block of plastic. Contrast of the plastic behind the tungsten is clearly seen in the line out. Also note, the signal through just tungsten (130 cts/pixel) is lower than through just plastic (175 cts/pixel)

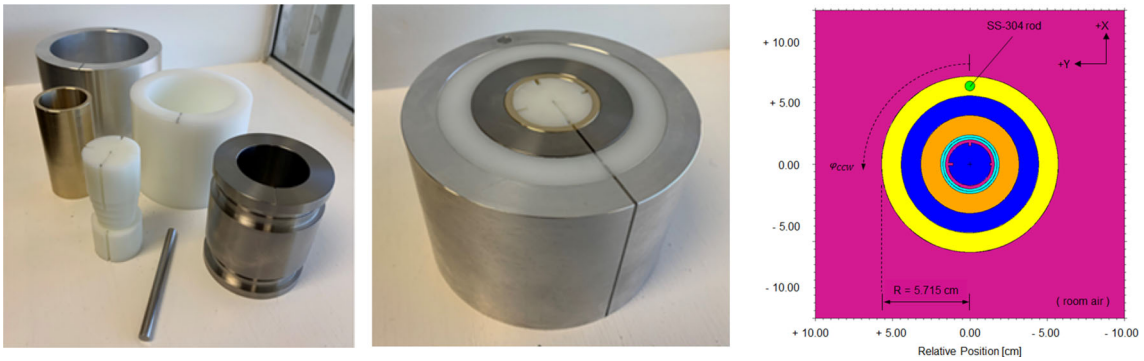

Fig. 15 Photographs of the XR05 cylindrical radiography test object disassembled (left), assembled (center), and MCNP model (right). The layers consist of a polyethylene center, brass cylinder, titanium cylinder, polyethylene cylinder, and aluminum cylinder with various machined grooves

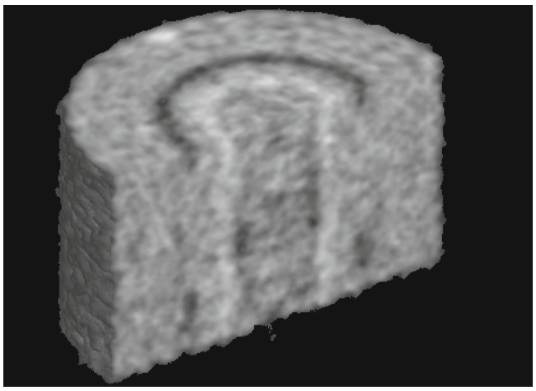

Fig. 16 Cross-sectional reconstruction of a 45 view DT neutron CT data set of the XR05

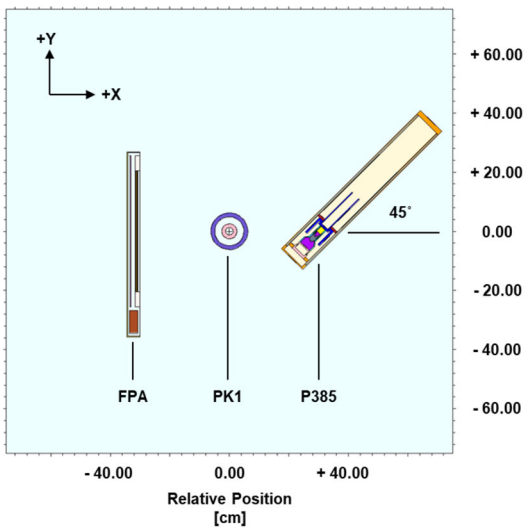

Fig. 17 MCNP model of the P 385 DT neutron generator, XRD imaging panel, and tungsten/polyethylene radiography test object

scintillator screen. As in the experiment, a 0.5 mm tantalum sheet was placed on the scintillator screen to block secondary photons. Detector blur correction was not included because most of the blur is due to the target spot size. The source output was modeled as a 7 mm diameter source spot as a square distribution and emitting 14.1 ± 0.375 MeV neutrons. The source head was oriented at 45° relative to the imaging axis.

Modeling the tungsten spherical shell plus polyethylene cylinder RTO shown in Fig. 11 proved to be a good test case to compare the modeling to the experimental image data. The MCNP simulation geometry is shown in Fig. 17 to match the experimental geometry. The source-to-object distance was 30.00 cm, and the object-to-detector distance was 31.00 cm for an M ~ 2.033: 1.

The initial simulation results did not account for about 6% of the image counts as evaluated within the central part of the image. This was initially attributed to an unknown neutron scatter contribution. After multiple iterations, several improvements and corrections were found and applied with good result. Adding in a more accurate model of the lift table and supports brought the simulation to within ~ 4% of the experimental results. Using the neutron monitor as illustrated in Fig. 10 to renormalize the open field measurement to the same neutron counts seen in the object image results in a flat field (I/I_0) image profile that improves the simulation image by ~ 1.57%. Adding room backscatter into simulated "total" images rather than the reverse further improves the flat field (I/I_0) image profiles by ~ 1.23%. Finally, including more accurate room details for floor, walls, ceiling, etc. reduced the discrepancy to just over 1%.

Figure 18 shows a side-by-side comparison of the experimental image (left) and the MCNP simulation (right) incorporating the experimental and simulation refinements described above. Figure 19 compares lineouts of the central region of the RTO for both experimental image and the simulation. The line-out agreement is within about 1.3%.

Imaging simulation of the XR05 object shown in Fig. 15 was also done with MCNP and is shown in Fig. 20 compared

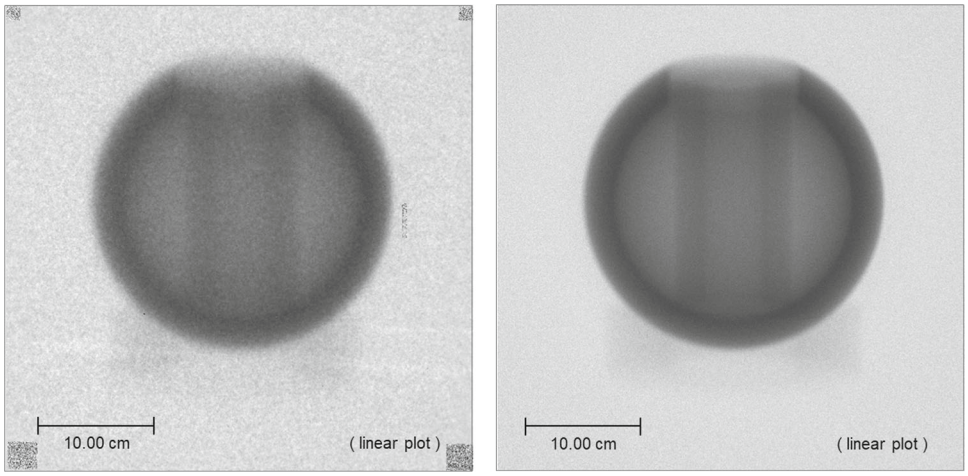

Fig. 18 Flat-fielded experimental image of tungsten/polyethylene object (left) and MCNP image (right)

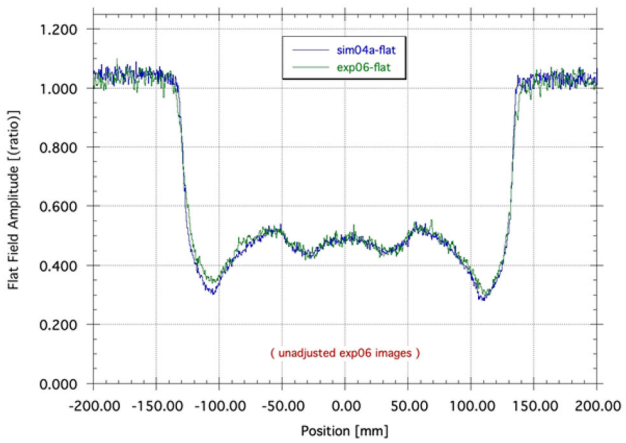

Fig. 19 Comparison of central line-out plot profile of experimental data and fully detailed MCNP model of the tungsten/polyethylene test object showing excellent agreement. Allowing an artificial χ^2 optimized additional scatter correction in the central region improves agreement by only 1.3%

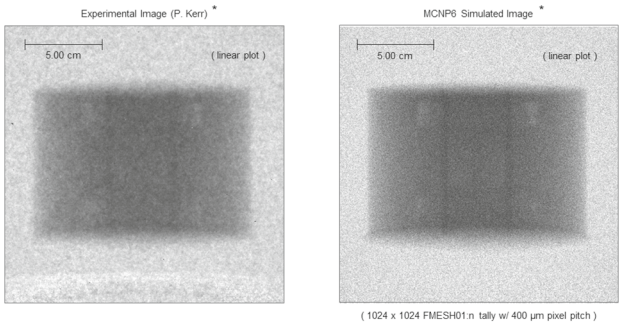

Fig. 20 Comparison of the experimental XR05 flat fielded image (left) compared to MCNP model (right)

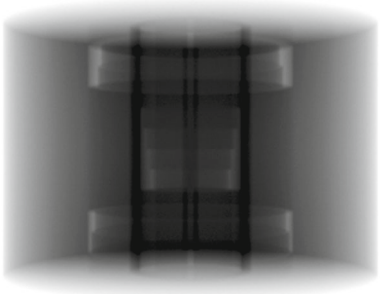

Fig. 21 MCNP model of XR05 showing improvement predicted using a neutron source with a 2 mm spot size

to the experimental image. While qualitatively in agreement and showing some of the expected features, the resolution and neutron source output is still limiting the image quality that can be obtained. To this point, the same MCNP model was used to predict the image quality when the neutron generator spot size is reduced from 7 to the 2 mm expected with the next-generator neutron generators. This potential improvement is shown in Fig. 21.

Conclusions

The value of fast-neutron imaging is not in matching the results of X-ray imaging, but in providing rough information on the interior of objects that cannot be imaged with X-rays. The signal-to-noise (S/N) of X-ray imaging is typically better than neutron imaging, and the S/N of thermal neutron imaging is typically better than fast-neutron imaging. The factors influencing S/N are source flux, beam collimation or spot size, and particle-induced scintillator light production. Fast neutrons have a much lower interaction cross-section in imaging screens than thermal neutrons or X-rays and therefore produce much less light. The thicker the screen, the more light produced, but the more the blurring and lower the image resolution. A standard scintillator for fast-neutron imaging is a ZnS(Cu) screen. At the maximum ZnS thickness

of 2–3 mm, which is limited by self-attenuation of scintillator light, the resolution is limited to 1–2 mm. Yet the light produced by fast neutrons in this scintillator is still 1000 × less than the equivalent imaging with X-rays. The methods to improve image quality addressed here are replacing the ZnS(Cu) screen with a higher light yield segmented scintillator, replacing the Thermo Scientific P 385 neutron generator with a smaller spot size, higher output Starfire nGen-400-DT-VIPS neutron generator, and techniques to mitigate digital panel noise. Practical applications of portable fast-neutron imaging are field radiography of items that cannot be moved to fixed imaging facilities and that have high-density casings around low-density materials. Some examples include inspection of concrete and welds for corrosion in bridges, vehicles, and other infrastructure, measurement of material levels in containers, and inspection of munitions or unknown packages.

The fast-neutron imaging system being developed here has demonstrated complementary information to X-ray radiography and the potential for a field-portable neutron imaging system. While providing lower resolution than X-ray radiography, the fast-neutron imaging system can produce contrast images of low-Z materials within high-Z materials not possible with portable low-energy X-ray imaging systems. The single-angle neutron radiographs acquired here were four minutes total imaging time, including two minutes of active neutron frames and two minutes of passive dark frames. The measurement time goal for a practical field-portable system, where larger objects and larger source to detector distances than used here are expected, is < 15 min.

We have demonstrated improvements in signal-to-noise of 3 × using panel-noise mitigation techniques. We also demonstrated a 6 × improvement in light production over the 2.4 mm ZnS(Cu) screen using the new SH-267 high light yield segmented scintillator. Future work is to produce several segmented 10 cm × 10 cm × 2.54 cm tiles of SH-267 to fill the 41 cm × 41 cm imaging panel. Advancements in neutron generator construction are expected to yield an additional factor of > 10 × in neutron production. Scintillator light production and neutron yield relate directly to improvements in signal-to-noise. Combined, the expected improvement in signal-to-noise is > 180x, better than the goal of 100x. In addition, new DT neutron sources will improve imaging resolution further with expected spot size reduction from 7–10 mm to 2–3 mm. Through MCNP simulations we successfully modeled room scatter effects in the tungsten shell data, and demonstrated the potential improvements to contrast and resolution with the expected advancements in portable neutron sources.

Acknowledgments This work was supported by the US DOE NNSA NA-22, NA-84, and LLNL-LDRD 20-SI-001, and was performed under the auspices of the U.S. Department of Energy by Lawrence Livermore National Laboratory under Contract DE-AC52-07NA27344. On behalf of all authors, the corresponding author states that there is no conflict of interest. Data is available on request.

References

1. Zuber, S. C. (2016). Applying practical neutron radiographic inspection to the department of army, Technical Report AREIS-TR-160052016, Nov. 2016.
2. Klann, R. T. (1996). Fast neutron (14.5 Mev) radiography: a comparative study, engineering division, argonne national laboratory, ANL/ED/CP-88443. In *Proceedings of the fifth world conference on neutron radiography*
3. R. Zboray, R. Adams, Z. Kis, Fast neutron radiography and tomography at a 10 MW research reactor beamline. Appl. Radiat. Isot. **119**, 43–50 (2017)
4. Bishnoi, S., Sarkar, P. S., Thomas, R. G., Patel, T., Gadkari, S. C. (2016) Fast neutron radiography with DT neutron generator. Indian National Seminar & Exhibition on Non-Destructive Evaluation NDE 2016, Dec, Thiruvananthapuram (NDE-India 2016), NDT.net 2017-06
5. Sowerby, B. D., Cutmore, N. G., Liu, Y., Peng, H., Tickner, J. R., Xie, Y., Zong, C. (2009). Recent developments in fast neutron radiography for the interrogation of air cargo containers. In *IAEA Conference*, Vienna, pp. 4–8 May 2009.
6. J.E. Eberhardt, S. Rainey, R.J. Stevens, B.D. Sowerby, J.R. Tickner, Fast neutron radiography scanner for the detection of contraband in air cargo containers. Appl. Rad. Isot. **63**, 179 (2005)
7. Osterloh, K. R. S., Bücherl, T., Hasenstab, A., Rädel, C., Zscherpel, U., Meinel, D., Weidemann, G., Goebbels, J., Ewert, U. (2007). Fast neutron radiography and tomography of wood as compared to photon based technologies, DIR 2007. In *International symposium on digital industrial radiology and computed tomography*, Lyon, France, June pp. 25–27.
8. R. Zboray, R. Adams, M. Morgano, Z. Kis, Qualification and development of fast neutron imaging scintillator screens. Nuclear Instruments and Methods in Physics Research A **930**, 142–150 (2019)
9. Chuirazzi, W. C., Oksuz, I., Kandlakunta, P., Massey, T. N., Brune, C. R., Cherepy, N. J., Martinez, H. P., Cao, L. (2018). Evaluation of polyvinyl toluene scintillators for fast neutron imaging. Submitted to Journal of Radioanalytical and Nuclear Chemistry 318: 543–551
10. Cherepy, N. J., Seeley, Z. M,. Hok, S., Schneberk, D., Kerr, P., O'Neal, S. P., Oksuz, I., Bisbee, M., Lei R. C., Payne, S. A., Sanner, R. D., Stone, G., Hobson, B. F., Guethlein, G., Hall, J., Stoneking, R., Mintz, J., McNamee, C., Thelin, P. A. (2020). Scintillators and detectors for MeV X-ray and neutron imaging. In *Proceedings SPIE, Hard X-Ray, gamma-ray, and neutron detector physics* XXII.
11. Nicolino, J., Hok, S., Cao, L. (2021). Fast neutron computed tomography of multi-material complex objects. In *Proceedings SPIE Hard X-Ray, gamma-ray, and neutron detector physics* XXIII, San Diego, CA, United States.